MESOSCOPIC PHYSICS

Observation of current whirlpools in graphene at room temperature

Marius L. Palm[1]†, Chaoxin Ding[1]†, William S. Huxter[1]†, Takashi Taniguchi[2], Kenji Watanabe[3], Christian L. Degen[1,4]*

Electron–electron interactions in high-mobility conductors can give rise to transport signatures resembling those described by classical hydrodynamics. Using a nanoscale scanning magnetometer, we imaged a distinctive hydrodynamic transport pattern—stationary current vortices—in a monolayer graphene device at room temperature. By measuring devices with increasing characteristic size, we observed the disappearance of the current vortex and thus verified a prediction of the hydrodynamic model. We further observed that vortex flow is present for both hole- and electron-dominated transport regimes but disappears in the ambipolar regime. We attribute this effect to a reduction of the vorticity diffusion length near charge neutrality. Our work showcases the power of local imaging techniques for unveiling exotic mesoscopic transport phenomena.

Transport phenomena in mesoscopic devices are governed by the relative distance separating carrier scattering events compared with the characteristic device size L. In a noninteracting system, once the device size becomes smaller than the momentum-relaxing scattering length l_{mr} set by collision events with impurities and phonons ($L \ll l_{mr}$), carriers move unimpeded until they are scattered off a device boundary. This ballistic regime is of great scientific interest and manifests itself, for example, in transverse magnetic focusing experiments (*1*) or through a quantized conductance in quantum point contacts (*2*).

In contrast, momentum-conserving collisions between carriers play a minor role in the transport of conventional metals, because they occur much less frequently than momentum-relaxing collisions (*3*, *4*). However, in materials where scattering events are scarce, such as encapsulated graphene and high-mobility Ga[Al]As heterostructures at intermediate temperatures, l_{mr} can approach or even surpass the carrier–carrier scattering length (l_{ee}) for a finite temperature range. Consequently, in a device satisfying $l_{ee} \ll L$, l_{mr}, transport properties become dominated by carrier–carrier interactions. This regime, governed by the collective behavior of interacting carriers, can give rise to peculiar transport features that are not expected from traditional diffusive or ballistic transport, such as viscosity (*5*) or even turbulence (*6*). Given its similarity to classical fluid flow, this transport regime is commonly referred to as the viscous or hydrodynamic regime.

Initial theoretical work on hydrodynamic electron transport predicted a decrease of the resistivity with increasing temperature in metallic wires (*7*). This effect, known as the Gurzhi effect, was first demonstrated experimentally in a Ga[Al]As heterostructure (*8*, *9*). Other hallmarks of hydrodynamic transport include the viscous Hall effect (*10*–*13*), su[illegible] ballistic conduction (*14*–*16*), flow without [illegible] Landauer-Sharvin resistance (*17*), Poiseuille flow in a channel (*18*–*22*), and Stokes flow around obstacles (*23*, *24*). One of the most notable predictions of hydrodynamic theory is the formation of stationary vortices (or whirlpools) (*5*, *25*–*29*), which has been indirectly confirmed by negative resistance measurements caused by current backflow (*30*–*32*). Recently, para-hydrodynamic vortices were shown to exist in tungsten ditelluride (WTe_2) at cryogenic temperatures through direct imaging (*33*). Although transport in this system is described by a hydrodynamic theory, the observed vortices do not originate from electron–electron interactions. Genuine electron-hydrodynamic vortices, although widely anticipated (*5*, *29*), have remained challenging to realize.

Here, we demonstrate direct imaging of stationary current whirlpools in a monolayer graphene (MLG) device at room temperature with scanning nitrogen-vacancy (NV) magnetometry (Fig. 1A). We studied the crossover regime from vortex-free to vortex flow (presence of a single whirlpool) and found that the vortex signature is most pronounced in the smallest devices and disappears upon increasing the device size. We observed the whirlpools

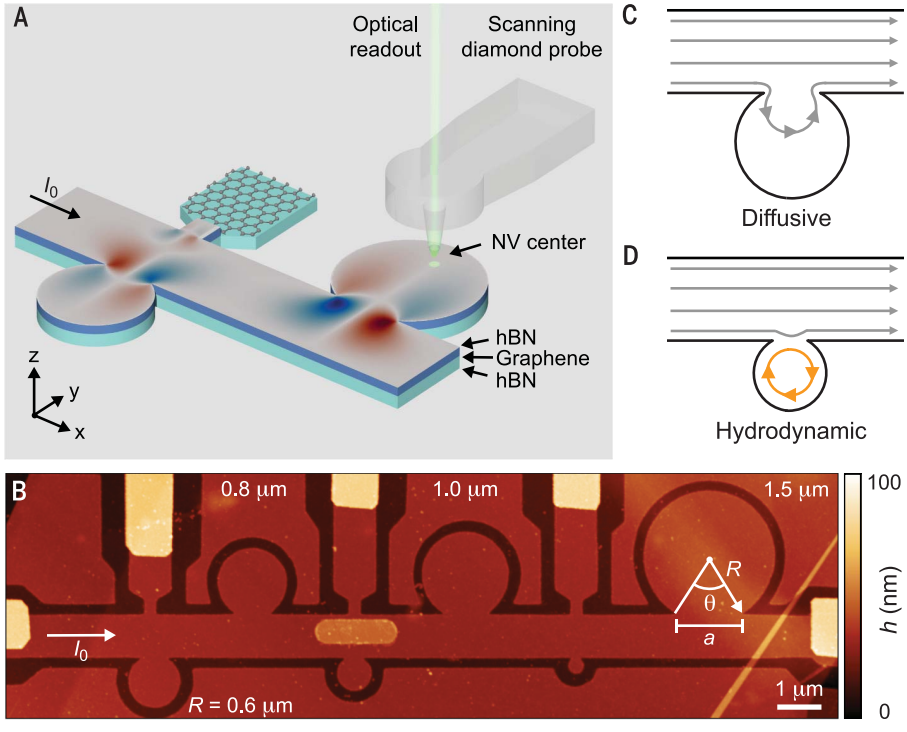

Fig. 1. Schematic of the scanning experiment. (**A**) Configuration of the encapsulated monolayer graphene (hBN-MLG-hBN) device and scanning nitrogen-vacancy magnetometer. hBN, hexagonal boron nitride. (**B**) Topography (atomic force microscopy) image of the investigated graphene device. The device consists of a main channel and disk-shaped side pockets of varying radius R. The disk opening is approximately $a \approx R$ ($\theta \approx 60°$ by design). Bright features are gold contacts. I_0 is the source-drain current. (**C**) Schematic of current flow in the diffusive regime. (**D**) In the hydrodynamic regime, current flow inside the disk reverses direction.

[1]Department of Physics, ETH Zurich, 8093 Zurich, Switzerland. [2]Research Center for Materials Nanoarchitectonics, National Institute for Materials Science, Tsukuba 305-0044, Japan. [3]Research Center for Electronic and Optical Materials, National Institute for Materials Science, Tsukuba 305-0044, Japan. [4]Quantum Center, ETH Zurich, 8093 Zurich, Switzerland.
*Corresponding author. Email: degenc@ethz.ch
†These authors contributed equally to this work.

in both electron and hole-dominated regimes, but not as the doping approached charge neutrality. Overall, our measurements are well explained by a hydrodynamic description and clearly rule out a purely diffusive theory.

Imaging of current whirlpools

The collective motion of a viscous electron fluid can be described by the Navier-Stokes equation in conjunction with the continuity equation (*3*, *18*)

$$\vec{J}(\vec{r}) - D_v^2 \nabla^2 \vec{J}(\vec{r}) + \sigma_0 \nabla\phi(\vec{r}) = 0 \quad (1)$$

$$\nabla \cdot \vec{J}\left(\vec{r}\right) = 0 \quad (2)$$

Here, the current density $\vec{J}(\vec{r})$ reflects the flow velocity subject to a potential gradient $\nabla\phi(\vec{r})$ and a viscous term $\nabla^2\vec{J}(\vec{r})$. D_v is the characteristic length scale describing vorticity diffusion, commonly referred to as the Gurzhi length, and σ_0 is the Drude conductivity (*18*). The Gurzhi length can further be related to microscopic scattering theory through the following equation (*13*, *14*)

$$D_v = \frac{1}{2}\sqrt{l_{ee} l_{mr}} \quad (3)$$

To resolve spatial signatures of viscous electron flow, the characteristic size of the device should be similar to or smaller than the Gurzhi length. For high-quality MLG at room temperature, l_{ee} is on the order of 0.2 μm (*11*, *34*), and $l_{mr} \sim 1.0$ μm (*35*), resulting in an expected D_v on the order of 0.2 μm.

Our MLG device consists of a uniform channel with disk-shaped side pockets (Fig. 1B). For this geometry, the critical length scale is mostly set by the disk opening a (*33*). When a is much larger than D_v, the channel current can enter the disk and produce a coflowing current inside the disk (Fig. 1C). The flow pattern is primarily governed by the potential gradient $\nabla\phi(\vec{r})$ and resembles diffusive transport. By contrast, when the disk opening is similar to or smaller than D_v, the laminar current through the main channel can no longer enter the disk; instead, a counterflowing vortex current appears mediated by momentum-conserving interactions (Fig. 1D). Therefore, the current direction in the disk—coflowing or counterflowing—serves as a hallmark to discriminate between diffusive and hydrodynamic transport.

To map the current distribution in the channel and disk, we imaged the current-generated magnetic field ~70 nm above the MLG sheet using a scanning NV magnetometer (*36*) (Fig. 1A). We used current amplitudes I_0 of 2 to 30 μA, which are sufficiently small to not heat the electron gas but still easily detectable by our magnetometer (*37*). To further enhance the sensitivity, we modulated the current at $f \sim 25$ to 65 kHz and synchronized it with a spin-echo detection of the spin sensor's quantum phase (*20*, *37*). A graphite back gate located ~24 nm beneath the graphene flake was used to tune the carrier type (electrons, holes) and concentration between approximately $\pm 2 \times 10^{12}$ cm^{-2}.

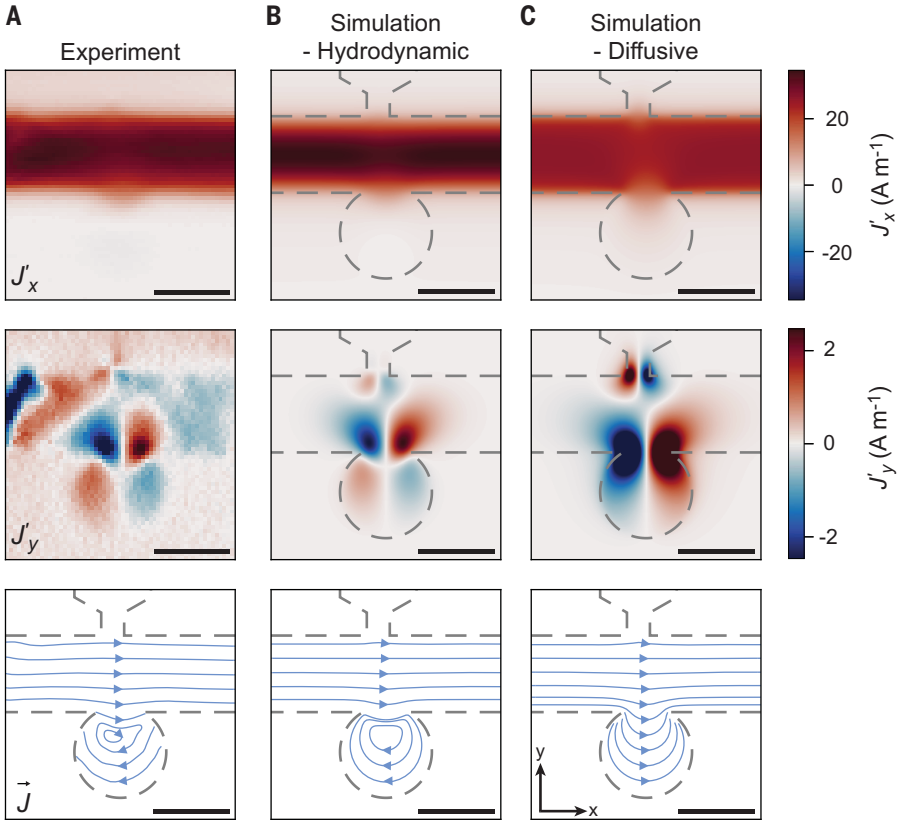

Fig. 2. Observation of current whirlpools. (**A**) Measured channel flow J'_x (top), transverse flow J'_y (middle), and velocity plot of the current density vector $\vec{J}$ (bottom) in the hole-doped regime ($n \approx -1.7 \times 10^{12}$ cm^{-2}). (**B**) Simulation of the same geometry using the hydrodynamic model ($D_v = 0.28$ μm). (**C**) Simulation using the diffusive model ($D_v = 0.001$ μm). Both simulations use a no-slip boundary condition. Simulated maps are low-pass filtered for direct comparison with the experimental J'_x and J'_y maps (*38*). The dashed lines indicate the device edges. Scale bars, 1 μm. Measurements were taken at room temperature.

Even deep into the hydrodynamic regime, the vortex current is expected to reach only a few percent of the total current I_0. To discern the subtle vortex texture from the dominating channel flow, we aligned the device such that the channel current flowed along x, while the transverse currents in and out of the disk flowed along y. Consequently, we could use the two magnetic field components $B_x \sim +\mu_0 J'_y/2$ and $B_y \sim -\mu_0 J'_x/2$ to obtain separate maps for each current direction. Here, J'_x and J'_y are the low pass–filtered (owing to the NV standoff distance) sheet current densities with units of ampere per meter; $\mu_0 = 4\pi \times 10^{-7}$ T·m/A. See (*38*) for a discussion of the current reconstruction.

Figure 2A shows experimental maps of the current flow in the $R = 0.6$ μm disk, together with numerical simulations of Eqs. 1 and 2 for the hydrodynamic case (Fig. 2B) and the diffusive case (Fig. 2C), respectively. The sign and shape of the measured J'_y matches the counterflow of the viscous simulation. In addition to the vortex feature in the $R = 0.6$ μm disk, the experiment also reproduces the smaller current vortex in the lateral voltage probe and the reduction in J'_x along the channel edges [indicative of Poiseuille flow; see (*38*)]. The hallmark sign of J'_y and the detailed agreement between simulated and experimental maps constitute the first piece of evidence that transport is governed by electron hydrodynamics in our doped MLG device.

Transition from viscosity to diffusion-dominated transport

To further support the hydrodynamic model, we imaged current flow in several disks (R = 0.6 to 1.5 μm) at a fixed carrier density of $n \approx -1.7 \times 10^{12}$ cm^{-2} (Fig. 3A). Vortices are present up to $R = 1.0$ μm and absent for the largest disk ($R = 1.5$ μm), indicating the transition out of a viscosity-dominated transport regime. Assuming a device-independent Gurzhi length of $D_v = 0.28$ μm, we accurately reproduced this transition with numerical simulations (Fig. 3B).

The disappearance of the vortex with larger disk size may be explained with an intuitive

picture (Fig. 3C): As R increases, so does the disk opening $a \approx R$ (Fig. 1B). When a is small, the channel current cannot enter the disk because viscosity suppresses the in- and outflowing currents; meanwhile, a vortex is generated in the disk through momentum transfer (Fig. 3C, left). As a approaches the critical opening $a_{crit} \approx 4.7\, D_v$ (*33*), current starts entering the disk, and the vortex fades (Fig. 3C, middle). Above a_{crit}, the disk current reverses direction and flows as is expected from diffusive transport (Fig. 3C, right). Because the flow pattern depends on the ratio a/D_v, we can estimate D_v by plotting the normalized transverse current density extracted symmetrically around the disk center as a function of $R \approx a$ (Fig. 3, D and E). Whereas we find excellent agreement for the larger disks, our model underestimates the vortex flow for the smallest disk (R = 0.6 μm). The deviation is likely caused by the assumption of a no-slip boundary condition; refined simulations with a finite slip length and complementary lattice Boltzmann simulations both predict increased counterflow for smaller disks (fig. S13).

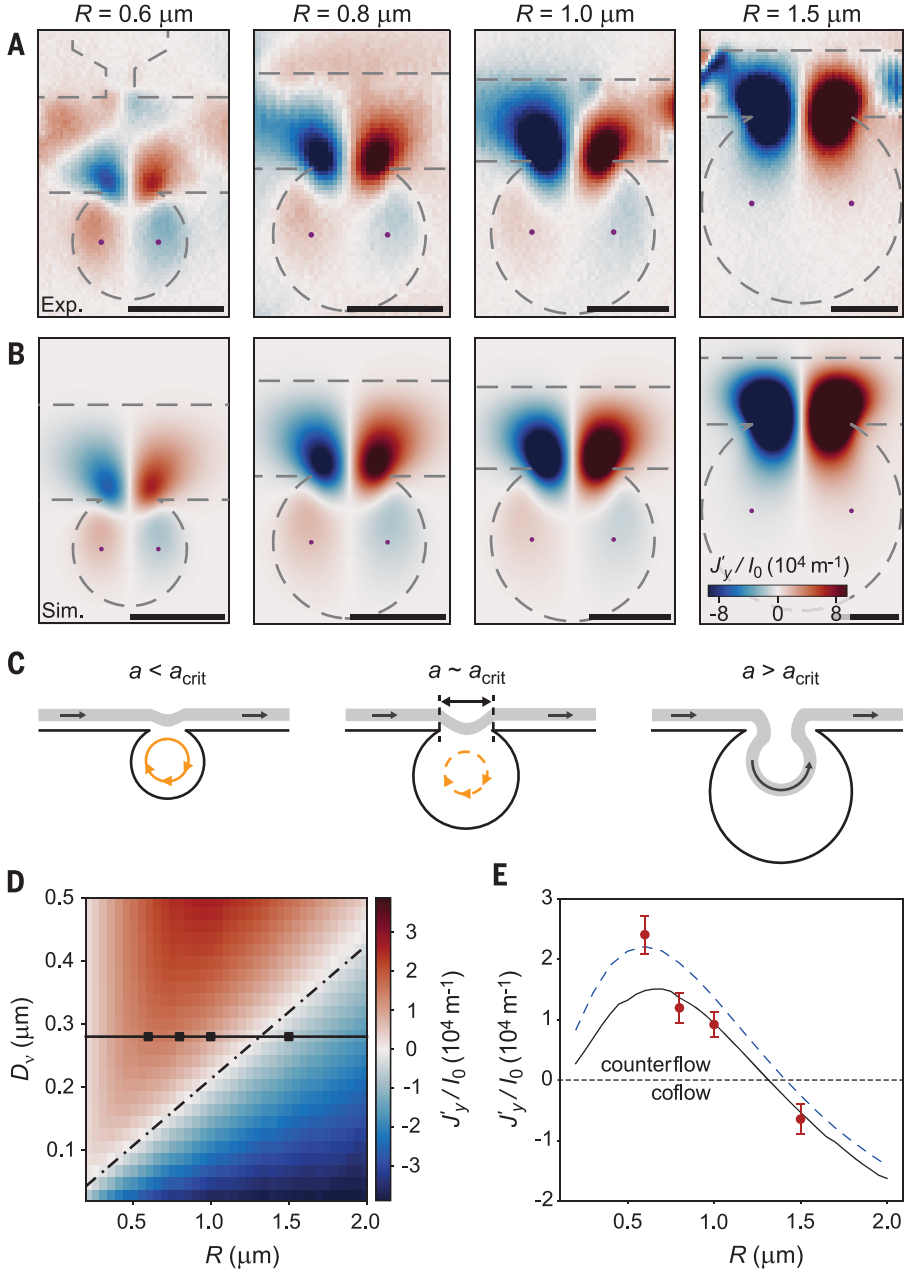

Fig. 3. Disk size determines the transport regime. (**A** and **B**) Transverse flow J'_y as a function of disk radius R. Top row (A) shows the experimental data and bottom row (B) shows the simulation using D_v = 0.28 μm with a no-slip boundary condition. All plots are normalized by the device current I_0. Scale bars, 1 μm. (**C**) Schematic illustrating the transition from vortex flow to vortex-free flow. (**D**) Magnitude of the backflow as a function of disk size and Gurzhi length (numerical simulation). Plotted is the transverse current density $J'_y := \left[J'_y(-R/2, 0) - J'_y(R/2, 0)\right]/2$ at locations (±R/2,0) relative to the center of the disk, marked by dots in (A) and (B). The black squares are from the simulations in (B). The horizontal center line corresponds to D_v = 0.28 μm. The dash-dotted line indicates the critical device size $R_{crit} \approx a_{crit}$ where J'_y changes sign. (**E**) Transverse current density J'_y plotted as a function of R. Red dots are the experimental data extracted from the maps in (A) (error bars are two standard deviations). Curves correspond to simulations using D_v = 0.28 μm assuming a no-slip boundary condition (solid black line) and a finite slip length (l_b = 81 nm, blue dashed line), respectively (*38*). Measurements were taken at room temperature.

Hole and electron carriers

We next turned our attention to the carrier density dependence of the vortex flow. Transport models for graphene predict that both l_{mr} and l_{ee} vary with carrier density (*39*–*41*), thus $D_v \propto \sqrt{l_{ee} l_{mr}}$ should also depend on n. Figure 4A shows flow patterns for the R = 0.6 μm disk recorded for hole doping at $n \approx -0.9 \times 10^{12}$ cm^{-2}, near the charge neutrality point (CNP), and for electron doping at $n \approx 0.9 \times 10^{12}$ cm^{-2}. Vortex flow is observed in both hole-dominated and electron-dominated regimes. Notably, however, the current backflow disappears near charge neutrality.

For a more quantitative analysis, we recorded a series of magnetic field maps for varying carrier densities and fit them with numerical simulations to extract values for D_v. Details regarding these simulations, including the implementation of a finite slip length boundary condition (*18*, *42*), are discussed in (*38*). The resulting values for D_v are plotted as a function of n in Fig. 4C. The data show a strong reduction of D_v near the CNP; D_v is approximately constant away from charge neutrality. Consistent with previous observations (*20*, *22*), we further observed a slight tendency for D_v to decrease for large (hole) doping. Note that around the CNP, the data are still best described by a hydrodynamic model with nonvanishing D_v, as opposed to a fully diffusive model (fig. S15).

The strong reduction of the Gurzhi length D_v near the CNP, which has also been observed in a previous imaging experiment (*43*), can be explained by a reduction of the microscopic scattering lengths. In the low-density Fermi liquid regime near the CNP, charged impurity scattering is likely to limit the conductivity in our device ($\sigma_0 \propto n$) (*39*, *44*). Consequently, the mean free path with respect to momentum-relaxing interactions $l_{mr} = \frac{h}{2e^2}\frac{\sigma_0}{\sqrt{\pi n}}$ becomes proportional to $\sqrt{n}$. Furthermore, l_{ee} scales approximately as $\sqrt{n}$ (*11*, *32*). Therefore, D_v is expected to increase with carrier density near charge neutrality. In the ambipolar regime, current-relaxing electron–hole collisions need

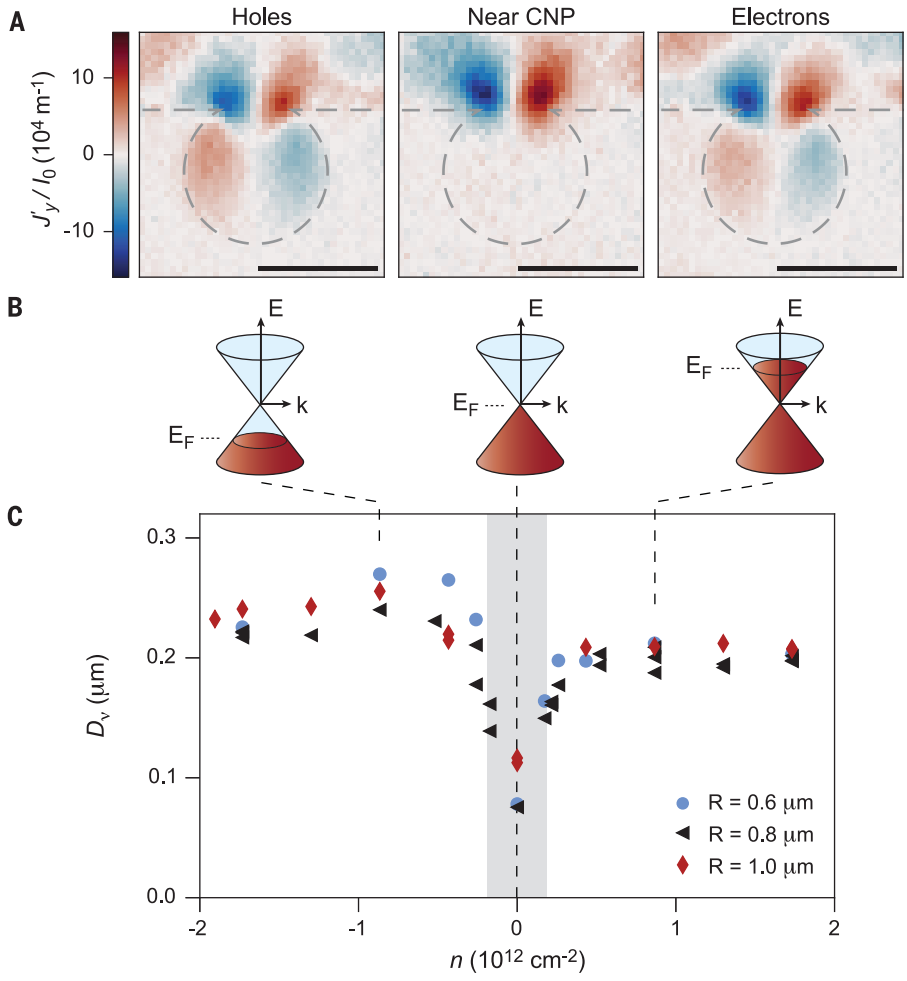

Fig. 4. Carrier dependence of the Gurzhi length. (**A**) Experimental J'_y flow for hole doping at $n \approx -0.9 \times 10^{12}$ cm^{-2} (left), near charge neutrality (middle), and for electron doping at $n \approx 0.9 \times 10^{12}$ cm^{-2} (right) for the $R = 0.6$ μm disk. Scale bars, 1 μm. (**B**) Schematic representation of the electronic band structure and location of the Fermi energy E_F for the scans shown in (A). (**C**) Gurzhi length D_v as a function of carrier density n. Corresponding plots for the slip length l_b and fits of the channel flow profiles are shown in figs. S3 and S4, respectively. The gray region indicates the ambipolar transport regime [$|E_F| \leq 2k_BT$, where k_B is the Boltzmann constant; see (*38*)]. The uncertainties of D_v values are around ±0.025 μm and are dominated by systematic errors caused by an imprecise knowledge of the device geometry [see (*38*) and fig. S6]. Measurements were taken at room temperature.

to be accounted for (*45*, *46*), and more-elaborate transport models may be required to describe the electronic transport accurately (*47*) and to connect the fitted values for D_v to the microscopic scattering lengths.

Curiously, we find that D_v is slightly larger for holes than for electrons. This carrier asymmetry is also evident by a mildly increased vortex flow for holes in the $R = 0.6$ μm disk (Fig. 4A). In addition, we observe an electron–hole inequality in the smallest investigated structure ($R = 0.2$ μm; fig. S14). Further evidence for a carrier asymmetry is provided by a fit to the current flow profile along the main channel, which is expected to follow the Poiseuille law. Interestingly, these fits yield D_v values for holes that are almost one-half the size of the vortex fits (fig. S4A). By contrast, D_v values for electrons are similar to those extracted from the vortex fits. Such electron–hole asymmetries are not expected from theory and merit further investigation. A possible explanation is a carrier type–dependent doping at the device edge, which would manifest itself in modified boundary conditions (*48*).

Discussion and outlook

Our experiments demonstrate that hydrodynamic whirlpools mediated by electron–electron interactions can be observed in high-mobility materials where $l_{mr} > l_{ee}$. The reversal of the current direction provides a clear spatial hallmark of hydrodynamic transport compared with other signatures, such as Poiseuille flow (*20*). Additionally, unlike the intermediate temperatures ($T \lesssim$ 200 K) required to observe hydrodynamic flow through a constriction (*43*), we find clear hydrodynamic signatures at room temperature, likely because of our smaller device geometry.

Although vortex-like features can also emerge in the ballistic regime (*29*, *33*), this is unlikely in our case for several reasons: first, to be dominated by ballistic effects, l_{ee} would need to be comparable or larger than the disk diameter, which is $2R \approx 2$ μm for the largest disk where we observe a current whirlpool (Fig. 3A). This value is an order of magnitude larger than previously reported $l_{ee} \sim 0.1$ to 0.25 μm at room temperature (*11*, *22*). Second, vortex flow patterns in the ballistic regime, although possible (*29*, *33*), are expected to deviate from those predicted by the hydrodynamic model. Yet we observe detailed agreement between our experimental data and the hydrodynamic simulation (Fig. 3). Because the transition from the hydrodynamic to the ballistic regime is smooth (*19*, *29*), however, a minor ballistic contribution to the flow pattern cannot be ruled out for the smallest disks ($R \lesssim 0.6$ μm).

Further studies will be needed to investigate the nature of boundary scattering in more detail, especially in view of the observed electron–hole asymmetry. Our data suggest that some edge defects may only affect transport for a single carrier type (fig. S14), potentially because of edge doping (*48*). More work is required to gauge whether a simple boundary condition using a single parameter (the slip length l_b) is sufficient to describe these effects. Corresponding experimental studies would benefit from lower temperatures, where the slip length is larger (*42*), or a smaller device size, where boundary effects are more prominent. Beyond graphene monolayers, bilayer graphene is a next obvious candidate, as the steeper rise of l_{ee} with carrier density (*32*, *41*), lower viscosity (*30*), and potentially dominant electron–hole collisions near charge neutrality (*45*) prominently alter the transport physics. Although bilayer graphene has been shown to exhibit a hydrodynamic transport regime (*30*, *32*), it has thus far eluded verification through scanning methods (*37*). Finally, an exciting prospect is the imaging of nonlinear hydrodynamic effects, such as preturbulence (*49*, *50*) and turbulence (*6*), which may be possible with NV centers by means of relaxometry measurements (*51*, *52*).

REFERENCES AND NOTES

1. S. Chen *et al.*, *Science* **353**, 1522–1525 (2016).
2. B. J. van Wees *et al.*, *Phys. Rev. Lett.* **60**, 848–850 (1988).
3. A. Lucas, K. C. Fong, *J. Phys. Condens. Matter* **30**, 053001 (2018).
4. B. N. Narozhny, *Riv. Nuovo Cim. Soc. Ital. Fis.* **45**, 661–736 (2022).
5. L. Levitov, G. Falkovich, *Nat. Phys.* **12**, 672–676 (2016).
6. D. Di Sante *et al.*, *Nat. Commun.* **11**, 3997 (2020).
7. R. N. Gurzhi, *Sov. Phys. Usp.* **11**, 255–270 (1968).
8. L. W. Molenkamp, M. J. M. de Jong, *Phys. Rev. B* **49**, 5038–5041 (1994).
9. M. J. M. de Jong, L. W. Molenkamp, *Phys. Rev. B* **51**, 13389–13402 (1995).
10. A. I. Berdyugin *et al.*, *Science* **364**, 162–165 (2019).
11. M. Kim *et al.*, *Nat. Commun.* **11**, 2339 (2020).

12. T. Scaffidi, N. Nandi, B. Schmidt, A. P. Mackenzie, J. E. Moore, *Phys. Rev. Lett.* **118**, 226601 (2017).
13. F. M. D. Pellegrino, I. Torre, M. Polini, *Phys. Rev. B* **96**, 195401 (2017).
14. H. Guo, E. Ilseven, G. Falkovich, L. S. Levitov, *Proc. Natl. Acad. Sci. U.S.A.* **114**, 3068–3073 (2017).
15. R. Krishna Kumar *et al*., *Nat. Phys.* **13**, 1182–1185 (2017).
16. L. V. Ginzburg *et al*., *Phys. Rev. Res.* **3**, 023033 (2021).
17. C. Kumar *et al*., *Nature* **609**, 276–281 (2022).
18. I. Torre, A. Tomadin, A. K. Geim, M. Polini, *Phys. Rev. B* **92**, 165433 (2015).
19. J. A. Sulpizio *et al*., *Nature* **576**, 75–79 (2019).
20. M. J. H. Ku *et al*., *Nature* **583**, 537–541 (2020).
21. U. Vool *et al*., *Nat. Phys.* **17**, 1216–1220 (2021).
22. W. Huang *et al*., *Phys. Rev. Res.* **5**, 023075 (2023).
23. A. Lucas, *Phys. Rev. B* **95**, 115425 (2017).
24. G. M. Gusev, A. S. Jaroshevich, A. D. Levin, Z. D. Kvon, A. K. Bakarov, *Sci. Rep.* **10**, 7860 (2020).
25. F. M. D. Pellegrino, I. Torre, A. K. Geim, M. Polini, *Phys. Rev. B* **94**, 155414 (2016).
26. G. Falkovich, L. Levitov, *Phys. Rev. Lett.* **119**, 066601 (2017).
27. K. A. Guerrero-Becerra, F. M. D. Pellegrino, M. Polini, *Phys. Rev. B* **99**, 041407 (2019).
28. S. Danz, B. N. Narozhny, *2D Materials* **7**, 035001 (2020).
29. K. G. Nazaryan, L. Levitov, arXiv:2111.09878 [cond-mat.mes-hall] (2021).
30. D. A. Bandurin *et al*., *Science* **351**, 1055–1058 (2016).
31. B. A. Braem *et al*., *Phys. Rev. B* **98**, 241304 (2018).
32. D. A. Bandurin *et al*., *Nat. Commun.* **9**, 4533 (2018).
33. A. Aharon-Steinberg *et al*., *Nature* **607**, 74–80 (2022).
34. A. Principi, G. Vignale, M. Carrega, M. Polini, *Phys. Rev. B* **93**, 125410 (2016).
35. L. Wang *et al*., *Science* **342**, 614–617 (2013).
36. K. Chang, A. Eichler, J. Rhensius, L. Lorenzelli, C. L. Degen, *Nano Lett.* **17**, 2367–2373 (2017).
37. M. L. Palm *et al*., *Phys. Rev. Appl.* **17**, 054008 (2022).
38. See supplementary materials for additional information.
39. S. Das Sarma, S. Adam, E. H. Hwang, E. Rossi, *Rev. Mod. Phys.* **83**, 407–470 (2011).
40. Q. Li, S. Das Sarma, *Phys. Rev. B* **87**, 085406 (2013).
41. D. Y. H. Ho, I. Yudhistira, N. Chakraborty, S. Adam, *Phys. Rev. B* **97**, 121404 (2018).
42. E. I. Kiselev, J. Schmalian, *Phys. Rev. B* **99**, 035430 (2019).
43. A. Jenkins *et al*., *Phys. Rev. Lett.* **129**, 087701 (2022).
44. C. R. Dean *et al*., *Nat. Nanotechnol.* **5**, 722–726 (2010).
45. Y. Nam, D. Ki, D. Soler-Delgado, A. F. Morpurgo, *Nat. Phys.* **13**, 1207–1214 (2017).
46. L. Fritz, T. Scaffidi, arXiv:2303.14205 [cond-mat.str-el] (2023).
47. B. N. Narozhny, I. V. Gornyi, M. Titov, *Phys. Rev. B* **104**, 075443 (2021).
48. A. W. Barnard *et al*., *Nat. Commun.* **8**, 15418 (2017).
49. M. Mendoza, H. J. Herrmann, S. Succi, *Phys. Rev. Lett.* **106**, 156601 (2011).
50. A. Gabbana, M. Polini, S. Succi, R. Tripiccione, F. M. D. Pellegrino, *Phys. Rev. Lett.* **121**, 236602 (2018).
51. S. Kolkowitz *et al*., *Science* **347**, 1129–1132 (2015).
52. A. Ariyaratne, D. Bluvstein, B. A. Myers, C. A. Bleszynski Jayich, *Nat. Commun.* **9**, 2406 (2018).
53. M. L. Palm *et al*., Zenodo (2024); http://doi.org/10.5281/zenodo.10124549.

ACKNOWLEDGMENTS

The authors thank M. Markham (Element Six) for providing ^{12}C diamond material; J. Rhensius (QZabre) for nanofabrication; the Ensslin group; the FIRST Lab; the Euler computer cluster at ETH Zurich for access to their instrumentation; E. Zeldov, L. Ginzburg, K. Ensslin, T. Ihn, S. Ernst, and K. Herb for helpful discussions; and A. Eichler and J. Rhensius for help with the illustration in Fig. 1. **Funding:** This work was supported by the European Research Council through ERC CoG 817720 (IMAGINE); the Swiss National Science Foundation (SNSF) through the National Centre of Competence in Research in Quantum Science and Technology (NCCR QSIT), grant 51NF40-185902; and the Advancing Science and TEchnology thRough dIamond Quantum Sensing (ASTERIQS) program, grant 820394, of the European Commission. K.W. and T.T. acknowledge support from the JSPS KAKENHI (grants 20H00354, 21H05233, and 23H02052) and the World Premier International Research Center Initiative (WPI), MEXT, Japan. **Author contributions:** C.L.D. and M.L.P. conceived of the experiment. M.L.P., C.D., and W.S.H. carried out experiments. M.L.P. and C.D. performed the data analysis. C.D. and M.L.P. performed macroscopic simulations, and W.S.H. performed Boltzmann simulations. M.L.P. fabricated the sample. T.T. and K.W. provided the hexagonal boron nitride. M.L.P., C.D., W.S.H., and C.L.D. wrote the manuscript. All authors discussed the results. **Competing interests:** The authors have no conflicts to disclose. **Data and materials availability:** All data and software are available in the manuscript or the supplementary materials or are deposited at Zenodo (*53*).

SUPPLEMENTARY MATERIALS

science.org/doi/10.1126/science.adj2167
Materials and Methods
Supplementary Text
Figs. S1 to S15
References (*54*–*70*)

Submitted 13 June 2023; accepted 20 March 2024
10.1126/science.adj2167